Absorption Properties of Supercooled Liquid Water between 31 and 225 GHz: Evaluation of Absorption Models Using Ground-Based Observations

STEFAN KNEIFEL AND STEPHANIE REDL

Hans Ertel Centre for Weather Research, Climate Monitoring Branch, University of Cologne, Cologne, Germany

EMILIANO ORLANDI AND ULRICH LÖHNERT

Institute for Geophysics and Meteorology, University of Cologne, Cologne, Germany

MARIA P. CADEDDU

Argonne National Laboratory, Argonne, Illinois

DAVID D. TURNER

NOAA/National Severe Storms Laboratory, Norman, Oklahoma

MING-TANG CHEN

Academia Sinica Institute of Astronomy and Astrophysics, Taipei, Taiwan

(Manuscript received 28 June 2013, in final form 3 December 2013)

ABSTRACT

Microwave radiometers (MWR) are commonly used to quantify the amount of supercooled liquid water (SLW) in clouds; however, the accuracy of the SLW retrievals is limited by the poor knowledge of the SLW dielectric properties at microwave frequencies. Six liquid water permittivity models were compared with ground-based MWR observations between 31 and 225 GHz from sites in Greenland, the German Alps, and a low-mountain site; average cloud temperatures of observed thin cloud layers range from 0° to −33°C. A recently published method to derive ratios of liquid water opacity from different frequencies was employed in this analysis. These ratios are independent of liquid water path and equal to the ratio of α_L at those frequencies that can be directly compared with the permittivity model predictions. The observed opacity ratios from all sites show highly consistent results that are generally within the range of model predictions; however, none of the models are able to approximate the observations over the entire frequency and temperature range. Findings in earlier published studies were used to select one specific model as a reference model for α_L at 90 GHz; together with the observed opacity ratios, the temperature dependence of α_L at 31.4, 52.28, 150, and 225 GHz was derived. The results reveal that two models fit the opacity ratio data better than the other four models, with one of the two models fitting the data better for frequencies below 90 GHz and the other for higher frequencies. These findings are relevant for SLW retrievals and radiative transfer in the 31–225-GHz frequency region.

1. Introduction

Supercooled liquid water (SLW; i.e., liquid water at temperatures below 0°C) is a frequent constituent of mixed-phase (e.g., Boudala et al. 2004) and snow-bearing clouds (Battaglia and Delanoë 2013). SLW inside clouds can be found down to −40°C (Heymsfield et al. 1991), and is frequently below −30°C (Turner 2005; Shupe 2011). SLW plays a fundamental role in cold cloud microphysical properties [e.g., Arctic mixed-phase clouds (Morrison et al. 2012)]; it also strongly influences the cloud radiative properties (Turner et al. 2007) that can cause dramatic changes of the surface energy budget (Bennartz et al. 2013).

Corresponding author address: Stefan Kneifel, Institute for Geophysics and Meteorology, University of Cologne, Pohligstrasse 3, 50969 Cologne, Germany.
E-mail: skneifel@meteo.uni-koeln.de

DOI: 10.1175/JAMC-D-13-0214.1

Quantitative estimates of path integrated SLW (SLWP) are typically obtained from spaceborne or ground-based microwave radiometers (MWRs). Typically, the frequency range between 20 and 35 GHz is used for SLWP retrievals. Unlike methods in the infrared, MWRs operating at this low-frequency region do not suffer from saturation effects or hydrometeor scattering, and thus it is possible to derive SLWP even from convective or snow-bearing clouds. However, in some regions like the Arctic, the sensitivity to very small amounts of SLWP is of particular interest since a cloud with an SLWP amount from 10 to 50 g m^{-2} dramatically changes its short- and longwave radiative properties (Turner et al. 2007). One possible way to significantly improve the sensitivity and accuracy of ground-based SLWP retrievals is to augment the combination of the standard low-frequency channels with higher-frequency channels up to 200 GHz (Crewell and Löhnert 2003; Cadeddu and Turner 2011) as long as the high-frequency channels are not saturated by water vapor or disturbed by snowfall scattering (Kneifel et al. 2010).

A fundamental prerequisite for any liquid water retrieval in the MW is an accurate absorption model, which is essentially a model of the complex permittivity of liquid water. Standard permittivity models approximate existing laboratory observations using interpolation functions that are based on a simplified physical model of the absorption process in the MW. The longstanding but still unsolved major issue for the supercooled temperature region is that there is only one laboratory dataset in which the liquid water absorption was measured down to −18°C, and this dataset only included observations at a single frequency of 9.61 GHz (Bertolini et al. 1982). For higher frequencies (i.e., between 10 and 1000 GHz), there are no laboratory observations of liquid water absorption for temperatures below −6°C (Ellison 2007). As a consequence, all currently available permittivity models extrapolate into the supercooled temperature region. Without additional data points in the low-temperature region, the uncertainties in the model extrapolations naturally increase with decreasing temperature.

The uncertainties in modeling the absorption properties of SLW directly transfer to uncertainties in the SLWP retrievals. Lipton et al. (1999) simulated synthetic MWR observations for artificial single-layer liquid clouds for both a spaceborne and a ground-based sensor. They compared the permittivity model from Ray (1972) and two different versions of the model described in Liebe et al. (1991). Standard retrieval coefficients for a ground-based two-channel MWR (20.6 and 31.6 GHz) and the spaceborne Special Sensor Microwave Imager (SSM/I; 19.35–85 GHz) were then applied to the simulated brightness temperatures T_B that were computed with the different permittivity models. The resulting maximum SLWP difference for a 1-km-thick cloud with a cloud-top temperature of −20°C was 42% for the SSM/I sensor retrieval when applying the simulated T_B from the three permittivity models; for the ground-based MWR retrieval and a cloud-top temperature of −30°C, the influence on the retrieved SLWP differed by 64%. In a more recent study by Cadeddu and Turner (2011), ground-based MWR observations between 23 and 170 GHz were compared with radiative transfer simulations that used four different permittivity models (Liebe et al. 1991, 1993; Ellison 2006; Stogryn et al. 1995) and the SLWP estimate from a collocated infrared interferometer using the method outlined by Turner (2005). For clouds warmer than −15°C the SLWP bias between the infrared interferometer and the MW retrieval using different frequency combinations up to 150 GHz was found to be negligible. For clouds colder than −15°C, the MW retrieval errors using frequencies up to 90 GHz did not exceed ~25% for their considered models [except Liebe et al. (1991), which leads to larger deviations]. However, the SLWP retrieval error introduced by the models if including frequencies up to 170 GHz was found to be as large as 50% for the Stogryn model and as high as 80% for Liebe et al. (1991). The findings from Lipton et al. (1999) and Cadeddu and Turner (2011) might seem to be in some aspects contradictory; however, the selection of permittivity models [e.g., the older and stronger deviating model from Ray (1972) was not included in the study by Cadeddu and Turner (2011)] and the approach for estimating the potential SLWP errors were different. Despite the difference in model selection and methodology, both studies reveal that retrieval errors strongly increase for cloud temperatures lower than −15°C, particularly if frequencies higher than 35 GHz are included.

In absence of reliable laboratory data, different approaches have been developed to utilize MWR observations from supercooled clouds to evaluate the various permittivity models and their extrapolations to supercooled temperatures. If the properties of the dry atmosphere, water vapor profile, and the amount of SLWP can be well characterized, the absorption coefficient can be directly derived from MWR observations. Cadeddu and Turner (2011) found with such an approach that all four considered permittivity models significantly overestimated the SLW absorption coefficient between 90 and 170 GHz. This overestimation leads directly to an increasing underestimation of SLWP with decreasing temperatures by any MWR retrieval. The analysis was, however, limited to clouds with SLWP lower than 60 g m^{-2} because of saturation effects in the infrared spectrometer at higher SLWP values.

If no independent SLWP estimates are available, the MWR can still be used for validation even though the absolute values of the absorption coefficient cannot directly be derived. Mätzler et al. (2010) presented an approach to utilize the differences in the temporal variability of the dry atmosphere, water vapor, and liquid water to separate the part of the signal that is solely due to SLW. Taking the ratio at two different frequencies of the typically much faster opacity changes due to SLW, the measured opacity ratio is equal to the ratio of the SLW mass absorption coefficient. Mätzler et al. (2010) applied this method to supercooled clouds down to −27°C and the relatively narrow frequency range between 21 and 31 GHz. Their measured opacity ratios were found to fit best by the Stogryn model; however, the influence of correlated water vapor fluctuations at these specific frequencies is relatively large because of the inclusion of frequencies close to the water vapor absorption line at 22.24 GHz.

In this study, we apply the basic method developed by Mätzler et al. (2010) to observations collected over a much wider frequency range between 31 and 225 GHz and temperatures down to −33°C, and compare the observational results with six different permittivity models. Furthermore, we combine observations from different MWRs located at three observational sites: an Arctic location at 3250 m altitude at Summit Station in central Greenland, a high-altitude site (2650 m) in the German Alps, and a wintertime dataset from a low-altitude mountain site (511 m) in southwest Germany. In section 2, we briefly describe the six permittivity models used in this study, compare their predicted mass absorption coefficients, and estimate the related SLWP error introduced by the deviating absorption models. Relevant information about the different sites, instrumentation, and MWR calibration is given in section 3. Furthermore, we describe in this section the methods used to derive the opacity ratios. The observed opacity ratios are compared to the model predictions at 10 frequency combinations in section 4. In addition to the opacity ratio comparison, we discuss a method to estimate the mass absorption coefficient for 31.4, 52.28, 150, and 225 GHz using predictions of the mass absorption coefficient at 90 GHz from a reference model. The conclusions of the study and an outlook for future studies are given in section 5.

2. Permittivity models for liquid water

In the frequency range from 31 to 225 GHz and assuming nonprecipitating cloud droplets (i.e., droplet diameter d smaller than 50 μm), the size parameter $x = \pi d/\lambda$ (where λ is the wavelength) is smaller than 0.1, and thus we can use the Rayleigh approximation to calculate the mass absorption coefficient α_L:

$$\alpha_L = \frac{6\pi\nu}{\rho_L c_l}\mathcal{J}\left(\frac{\epsilon - 1}{\epsilon + 2}\right), \tag{1}$$

where α_L is dependent on the frequency ν of the external electromagnetic field, the liquid water density ρ_L, and the complex permittivity of the fluid $\epsilon = \epsilon' + i\epsilon''$ with ϵ' and ϵ'' being the real and imaginary part of ϵ, respectively; c_l is the vacuum speed of light, and $\mathcal{J}$ symbolizes the imaginary part of the expression in parentheses. The permittivity models used in this study to calculate α_L apply different variants of the Debye function (Debye 1929) to interpolate the experimentally measured permittivity data. The complex Debye function is related to the underlying physical process of polarization due to an external electric field and describes the viscously damped thermal disordering of the molecular water dipoles after removal of the external field. This so-called relaxation process can be described with a characteristic relaxation time τ for a given fluid and temperature. The absorption of energy from an external electromagnetic field is thus a maximum if the frequency of the external field approaches $1/(2\pi\tau)$. The basic formulation of the Debye function (single Debye) is as follows:

$$\epsilon = \epsilon_\infty + \frac{\epsilon_s - \epsilon_\infty}{1 - i2\pi\nu\tau}. \tag{2}$$

The quantity ϵ_s is the permittivity for a static electric field whereas ϵ_∞ represents the permittivity at "infinite" frequency. The parameters τ, ϵ_s, and ϵ_∞ are usually fitted to the experimental data as functions of temperature T. The single Debye function (2) can be extended to include additional relaxation processes that can be caused by additional dipole structures in a solution. Theoretical simulations and experimental data indicate that pure liquid water comprises different polar structures implying more than one relaxation process. A detailed discussion of this topic and an analysis of the fit quality for different numbers of relaxation processes can be found in Ellison (2007). While the physical interpretation of additional relaxation processes is still controversial, most of the models used within this study use a double Debye function with two relaxation times τ_1 and τ_2:

$$\epsilon = \epsilon_\infty + \frac{\epsilon_s - \epsilon_1}{1 - i2\pi\nu\tau_1} + \frac{\epsilon_1 - \epsilon_\infty}{1 - i2\pi\nu\tau_2}. \tag{3}$$

The double Debye function contains the additional relaxation time τ_2 and a second fit parameter ϵ_1.

TABLE 1. Permittivity models for liquid water used within this study.

Reference	Abbreviation	Frequency range	T range	Interpolation formula (for MW region)
Ray (1972)	RAY	0–300 THz	−20°, . . . , +50°C	Single Debye/Cole–Cole
Liebe et al. (1991, 1993)	LIE	0–1 THz	"Atmospheric"	Double Debye
Stogryn et al. (1995)	STO	Not specified	Not specified	Double Debye
Meissner and Wentz (2004)	MEI	0–500 GHz	−20°, . . . , +50°C	Double Debye
Ellison (2006)	ELL06	0–500 GHz	0°, . . . , +30°C	Double Debye
Ellison (2007)	ELL07	0–25 THz	0°, . . . , +100°C	Triple Debye

a. Description of the permittivity models

In this study, we selected a broad range of published permittivity models for the comparison with our observations. The characteristics of the various models are summarized in Table 1. The valid temperature range of some models is limited to nonsupercooled conditions or temperatures higher than −20°C. However, in the supercooled temperature regime, all of them rely on a similarly sparse laboratory dataset. Based on the lack of laboratory data, every model can be seen as less or more trustworthy in the supercooled temperature regime. For this reason, we decided to compare all models in the same temperature range and accept the fact that some of them lie outside their specified temperature range. The model presented by Ray (1972) (RAY) is the oldest model in our comparison but was also the most widely used model before 1991. It provides interpolation formulas for a wide frequency range from 0 to 300 THz subdivided into seven spectral ranges. For the spectral range between 0.1- and 10-cm wavelengths (3–300 GHz), Ray used a single Debye function with a Cole–Cole modification (Cole and Cole 1941) to fit the relatively sparse experimental dataset.

New experimental data motivated Liebe et al. (1991) to compile an updated permittivity model; this permittivity model is currently widely used in the atmospheric community. Liebe et al. introduced a double Debye function since new experimental data at frequencies larger than 100 GHz revealed the inability of the single Debye function to fit the higher-frequency data. In a later paper, Liebe et al. (1993) corrected the original function allowing the parameter ϵ_∞ to be independent of temperature to avoid unrealistic results at frequencies above 100 GHz and temperatures between −20° and −40°C. The Liebe model (LIE) used in this study is the corrected version presented in Liebe et al. (1993); we further use their quadratic temperature-dependent fit for τ_1 instead of the exponential fit.

The more recent models by Stogryn et al. (1995) (STO), Meissner and Wentz (2004) (MEI), and Ellison (2006) (ELL06) are all based on double Debye functions. The differences between the models arise from different datasets used to fit the Debye parameters and different definitions of the parameter functions. For example, in MEI and STO the parameter function for the first relaxation time τ_1 contains a singularity at −45°C where τ_1 becomes infinite. This behavior was motivated by the assumption that all supercooled water droplets will be transformed to solid ice by spontaneous phase transition at these low temperatures. While MEI also includes this singularity for the second relaxation time τ_2, the STO model assumes τ_2 to be temperature independent, which has been mentioned to be rather unphysical by Mätzler et al. (2010).

For the most recent model by Ellison (2007) (ELL07), a comprehensive review of all available permittivity measurements was performed in combination with a comparison of different interpolation formulas. The most accurate interpolation formula for the laboratory dataset including measurements at microwave frequencies up to the far infrared region includes three Debye terms and two non-Debye terms for resonant effects in the far infrared.

A comparison of the six permittivity models in terms of mass absorption coefficient is shown in Fig. 1 for liquid water at 0° and −25°C. At 0°C and frequencies lower than 150 GHz, the various models agree relatively well. Even up to 300 GHz, only slight deviations of up to 15% can be found. The only exception is the Ray model, which starts to deviate at frequencies larger than 150 GHz, ultimately resulting in a 40% smaller mass absorption coefficient relative to the other models at 300 GHz. The situation is completely different in the supercooled temperature region. At −25°C, the models begin to substantially deviate from each other at frequencies above 30 GHz. The models show differences in mass absorption coefficients up to 70% at 300 GHz with the LIE, STO, MEI, and ELL06 models predicting significantly higher mass absorption values compared to RAY and ELL07 models. One reason for the increasing spread among the models with decreasing temperatures even at lower frequencies is the temperature dependence of the two relaxation processes. At 0°C, the

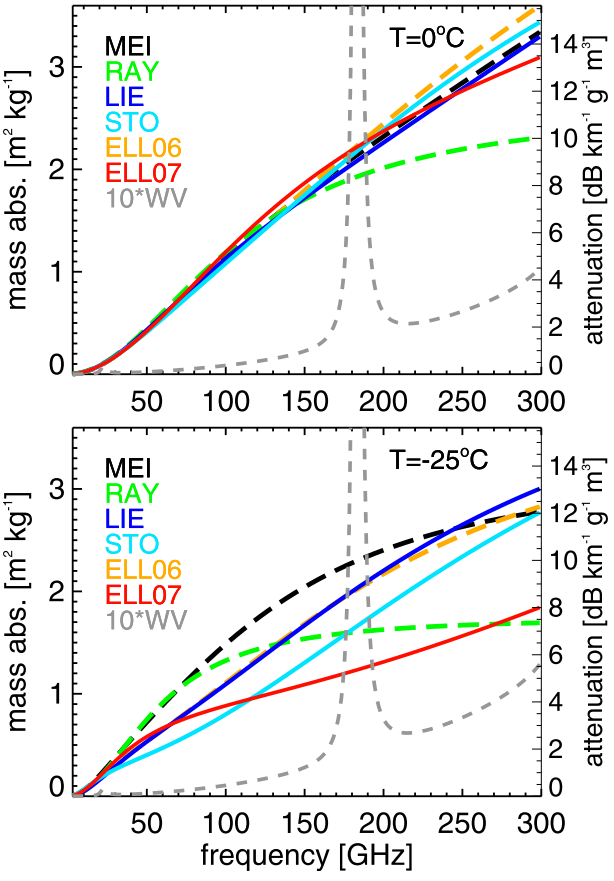

FIG. 1. Mass absorption coefficient ($m^2\,kg^{-1}$) as a function of frequency (GHz) as predicted by six different permittivity models for liquid water at (top) 0° and (bottom) −25°C. The right *y* axis shows the one-way liquid water attenuation [$dB\,km^{-1}\,(g\,m^{-3})^{-1}$], which can be interpreted as attenuation through a 1-km-thick liquid water cloud with constant liquid water content of $1\,g\,m^{-3}$. Details about the permittivity models (color coded) are given in Table 1 and in the text. For comparison, the mass absorption coefficient of water vapor at a constant pressure of 700 hPa multiplied by a factor of 10 is indicated by the gray dashed line.

absorption properties up to 100 GHz are dominated by the relatively well-known first relaxation process. At decreasing temperatures, the absorption properties become increasingly affected by the second relaxation process for which the temperature dependence is highly uncertain (Ellison 2007).

Basically, the reason for the large model deviations can be attributed to the extremely sparse experimental permittivity data in the supercooled temperature regime. While a large number of experimental datasets with liquid water measurements down to 0°C are available, the only dataset down to −18°C was collected at a single frequency (9.61 GHz) by Bertolini et al. (1982). For the higher-frequency range between 100 and 2000 GHz, only one laboratory dataset for the supercooled region down to −2°C is available from Ronne et al. (1997). This "no-data zone" for liquid water temperatures below −2°C and for frequencies above 20 GHz is the main source of uncertainty since all models have to extrapolate from the nonsupercooled temperatures into a widely unknown region of permittivity values.

b. *Implication of permittivity model uncertainties*

From a more practical point of view, it is worthwhile to discuss the impact of the permittivity model uncertainties on radar attenuation and on SLWP retrievals from MWR. Attenuation becomes increasingly important for cloud radars operating at higher frequencies (e.g., W-band cloud radars). The radar one-way attenuation due to SLWP absorption predicted by the different absorption models is indicated by the right *y* axis in Fig. 1. Attenuation values [$dB\,km^{-1}\,(g\,m^{-3})^{-1}$] can be interpreted as the attenuation that would result from a 1-km-thick cloud with constant temperature and a constant liquid water content of $1\,g\,m^{-3}$. The related liquid water path (LWP) of $1\,kg\,m^{-2}$ is relatively large and can usually only be found in convective clouds. For a 94-GHz cloud radar, all models predict a liquid water attenuation of about 4.5 dB at 0°C. However, for a supercooled cloud with a mean liquid water temperature of −25°C, the calculated attenuation values range from 3 dB for STO up to 6 dB for MEI.

We investigated the sensitivity of SLWP retrievals to the permittivity model uncertainties using a simple single-frequency physical retrieval for a ground-based, upward-looking MWR. Multifrequency SLWP retrievals are certainly more common and accurate; however, single-frequency retrievals provide a straightforward technique to characterize the influence of the permittivity model uncertainty on the derived SLWP. A typical winter profile of temperature, atmospheric pressure, and water vapor from our Alpine site (for further description of the site see next section) was combined with an artificial 1-km-thick liquid cloud layer with constant temperature and an initial $SLWP_{init}$ of $30\,g\,m^{-2}$. While the other atmospheric variables were kept constant, only the temperature of the cloud layer was varied between +5° and −35°C in steps of 5°C. The related T_B values were calculated with the RT4 radiative transfer model (Evans and Stephens 1995) and the different liquid water permittivity models. For small changes of SLWP (e.g., between 0 and $100\,g\,m^{-2}$) the relation between T_B and SLWP is linear. With the calculated sensitivity $\partial T_B/\partial \mathrm{SLWP}$, derived for a certain permittivity model and constant cloud temperature, we can write $\Delta \mathrm{SLWP} = (\partial T_B/\partial \mathrm{SLWP})^{-1}\Delta T_B$. In a similar way, we can also relate the T_B difference caused by two differing permittivity

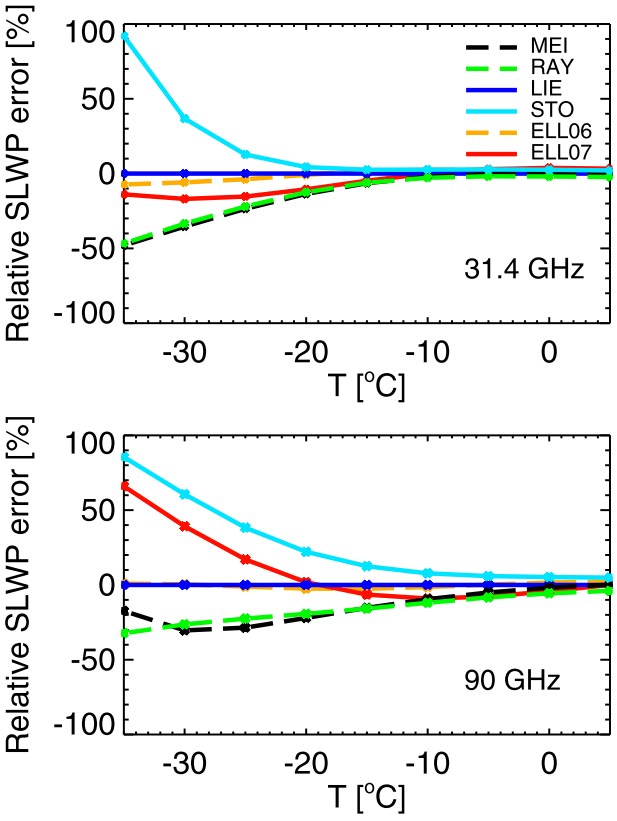

FIG. 2. Impact of the permittivity model uncertainties on retrieved SLWP for a ground-based MWR as function of cloud temperature T in °C. The relative SLWP error has been estimated with a simplified physical single-frequency retrieval for (top) 31.4 and (bottom) 90 GHz, assuming a typical winter atmosphere at the UFS and a homogeneous 1-km-thick cloud layer with a SLWP of 30 g m^{-2}. The different colors denote the various permittivity models similar to Fig. 1. It should be noted that the LIE model has been taken as the truth, and thus the SLWP deviations associated with the other models only illustrate the sensitivity of the SLWP retrieval to permittivity model uncertainties but are not indicating the real accuracy of a specific model.

models for a constant $\mathrm{SLWP}_{\mathrm{init}}$ to an SLWP uncertainty. Assuming the LIE model as the truth, the error in retrieved SLWP caused by a differing permittivity model (e.g., RAY) can be calculated with

$$\Delta\mathrm{SLWP} = \left(\frac{\partial T_{B,\mathrm{RAY}}}{\partial \mathrm{SLWP}}\right)^{-1} [T_{B,\mathrm{LIE}}(\mathrm{SLWP}_{\mathrm{init}}) - T_{B,\mathrm{RAY}}(\mathrm{SLWP}_{\mathrm{init}})]. \quad (4)$$

The relative SLWP errors $\Delta\mathrm{SLWP}/\mathrm{SLWP}_{\mathrm{init}}$ calculated for all permittivity models are shown in Fig. 2 as function of cloud temperature. It should be noted again that the retrieval "errors" shown in Fig. 2 and described in the following are always relative to our assumed truth (LIE) and are only intended to illustrate the general sensitivity of SLWP on temperature and model selection. The SLWP retrievals that only use 31.4-GHz data are largely insensitive to the permittivity model used in the retrieval for temperatures larger than −10°C. However, for lower temperatures, the retrieved SLWP is mostly underestimated by the permittivity models (up to −50% at −30°C); the only exception is the STO model, which largely overestimates SLWP by up to 95%. Retrievals for the more sensitive 90-GHz channel reveal relatively constant differences already in the 0° to −10°C temperature range. However, as the cloud temperatures become lower, the retrievals that use the ELL07 and STO models overestimate the SLWP by 60%–90%, while retrievals that use the other permittivity models underestimate SLWP by 15%–35% (again, relative to LIE). The range of bias errors in the retrieved SLWP using the different permittivity models is generally similar to the range found in earlier studies that used more complex multifrequency retrievals (Lipton et al. 1999).

3. Datasets and methods

The dataset used in this study is a combination of MWR measurements at 31, 52, 90, and 150 GHz from MWRs at three different sites, augmented by 225-GHz observations at one of the sites (Table 2). Auxiliary observations from cloud radar, lidar, and radio soundings (and/or numerical weather analysis data) are also available for all sites. These data are used to characterize the observed cloud types and atmospheric temperature and water vapor structure.

TABLE 2. Instrument characteristics of the MWRs and frequency channels used in this study.

MWR	Observation site	Center frequency (GHz)	Bandwidth (GHz)	Calibration accuracy (K)	Noise level (K)
HATPRO	UFS, FKB	31.4, 52.28	0.23, 0.23	2	0.5
HATPRO	SMT	31.4, 52.273	0.23, 0.178	2	0.5
DPR	UFS, FKB	90.0, 150.0	2.0, 2.0	3	1.0
MWR-HF	SMT	90.0, 150.0	2.0, 2.0	2	0.5
MWR-HF-225	SMT	225.0	1.0	2	1.0

a. Observational datasets

1) SUMMIT STATION, GREENLAND (SMT)

In 2010, a large suite of instrumentation was deployed at Summit Station in the center of the Greenland Ice Sheet (72.6°N, 38.5°W; 3250 m MSL) as part of the Integrated Characterization of Energy, Clouds, Atmospheric State, and Precipitation at Summit (ICECAPS) project (Shupe et al. 2013). The primary objective of this project is to collect a multiyear dataset that can be used to investigate important cloud–atmosphere properties and processes, and how these processes impact both the surface mass and energy budgets. The ICECAPS instrument suite includes a millimeter-wave cloud radar (MMCR), two polarization sensitive lidars, a ceilometer, an infrared interferometer, a sodar, an X-band precipitation sensor, two launches of Vaisala, Inc., RS92 radiosondes per day, and two MWRs. These two MWRs are the Humidity and Temperature Profiler (HATPRO), which provides observations of downwelling radiance in the spectral bands from 21 to 31 GHz and from 51 to 58 GHz (Rose et al. 2005), and a high-frequency (HF) radiometer, which makes measurements at 90 and 150 GHz. The latter system is very similar to the Dual Polarization Radiometer (DPR) that was utilized in earlier field experiments (Turner et al. 2009). A third MWR, which was manufactured by the same vendor who made the HATPRO and HF radiometers, provides downwelling radiance measurements at 225 GHz, and was deployed by the Academia Sinica Institute of Astronomy and Astrophysics (ASIAA) to characterize the viewing conditions at Summit Station for the possible deployment of a submillimeter astronomical telescope. We used 15 months of data from August 2011 to June 2012 and September to December 2012 in this analysis.

2) MOUNT ZUGSPITZE, GERMANY (UFS)

The second dataset analyzed was collected at the Environmental Research Station Schneefernerhaus (47.42°N, 10.98°E; 2650 m MSL) at the Zugspitze in the German Alps. The east–west alignment of the mountain massif leads to frequent blocking situations under north and northwesterly flow, resulting in strong lifting along the northern side of the mountain. As a result of the strong adiabatic cooling and orographically induced turbulence, strong and fast liquid water fluctuations at temperatures down to −20°C are frequently observed on the lee side of the mountain where the UFS is located. We analyzed a 3-month wintertime period (December 2008–February 2009) collected during the Toward an Optimal Estimation-Based Snowfall Characterization Algorithm (TOSCA) campaign (Löhnert et al. 2011). The site was equipped with two MWRs [both manufactured by Radiometer Physics (RPG)]: a HATPRO radiometer (similar to the one at SMT) owned by the UFS and a DPR owned by the Ludwig Maximilians University of Munich that makes observations at 90 and 150 GHz (Turner et al. 2009). Up to 90 GHz, both systems use direct detection receivers; only the 150-GHz channels of the DPR are heterodyne systems. Each MWR is equipped with heated blowers and camera surveillance systems to ensure data quality and to exclude time periods that have artifacts (e.g., ice on the radomes). Auxiliary data from the UFS are provided by a zenith-pointing 35.5-GHz microwave cloud radar (MIRA; Metek GmbH) and a ceilometer (CL31; Vaisala). No radiosondes are operationally launched at the UFS, thus we use analyses from the Consortium for Small Scale Modelling's (COSMO) operational weather forecast model COSMO-DE from the German Weather Service (2.8-km spatial and 1-h temporal resolution) for vertical thermodynamic profiles.

3) MURG VALLEY, BLACK FOREST, GERMANY (FKB)

The Atmospheric Radiation Measurement Program (ARM) Mobile Facility (AMF) was deployed as part of the Convective and Orographically Induced Precipitation Study (COPS; Wulfmeyer et al. 2008) and the general observation period (GOP; Crewell et al. 2008) in the Murg Valley (48.54°N, 8.40°E; 511 m MSL) in the Black Forest in southwest Germany from April to December 2007. We analyzed data from an autumn/winter period between October and December 2007 when thin layers of supercooled stratus clouds frequently occurred; this dataset complements the lower temperature data from SMT and UFS sites by providing measurements between 0° and −10°C. Although permittivity models do not deviate significantly in this temperature region, it is a valuable confirmation of our method since we expect that the observations will agree best with model predicted values in this "warm" temperature region. The FKB data also overlap in cloud temperature with data collected from the two other sites, providing an important consistency check between the three datasets. Two MWRs were deployed at the AMF site providing observations between 22 and 150 GHz: a HATPRO radiometer by the University of Cologne and the ARM two channel HF radiometer (Cadeddu et al. 2013) [both radiometers are very similar to those deployed at SMT (Table 2)]. From the large set of auxiliary observations provided by the AMF, our analysis used the observations from the 35-GHz cloud radar (MMCR), micropulse lidar (MPL), and the radiosonde ascents (Vaisala RS92) that were performed 4 times per day.

4) MICROWAVE RADIOMETER CALIBRATION

All radiometers (HATPRO, HF, DPR, 225-GHz MWR) are equipped with a comprehensive temperature stabilization (better than 30 mK) for the radiometric components (Rose et al. 2005). Absolute calibrations are performed for all radiometers according to the manufacturers' recommendations every few months using a liquid nitrogen target as a cold reference at ~77 K. The views of the liquid nitrogen target and the internal hot load are used to determine the system noise temperature, sensitivity (gain), and nonlinearity of the detector. Additionally, tip-curve calibrations (Han and Westwater 2000) were performed by all instruments at regular intervals; this calibration method also provides an absolute way to determine the gain and system noise of the radiometer. While the nonlinearity of the receiver can be assumed constant between two absolute calibrations, all radiometers use views of the internal ambient blackbody together with noise diodes (which were calibrated during the tip-curve process) every few minutes to update their gain and system noise calibrations.

b. *Opacity ratio method*

Our method of computing the opacity ratios between two frequencies is similar to the technique presented by Mätzler et al. (2010). Thus, we will only describe the most relevant parts of the idea and the differing aspects of our approach.

The total atmospheric opacity τ can be written as a sum of the contributions from dry air τ_D, water vapor τ_{WV}, and—in case of nonprecipitating, pure liquid water clouds—liquid water of suspended cloud droplets τ_L:

$$\tau = \tau_D + \tau_{WV} + \tau_L . \tag{5}$$

The single contributions, for example τ_L, are obtained for zenith viewing conditions by the integral

$$\tau_L = \int_0^{\mathrm{TOA}} \rho_L(z)\alpha_L[\nu, T(z)]\, dz , \tag{6}$$

with the liquid water concentration ρ_L, the frequency- and temperature-dependent liquid water mass absorption coefficient α_L, and the vertical height z.

The total opacity τ is usually derived with the radiative transfer equation in zenith direction and assuming a nonscattering atmosphere using the concept of a mean radiative temperature T_{mr} of the atmosphere (Ulaby et al. 1986). This approach usually assumes the validity of the Rayleigh–Jeans approximation (RJA), which allows us to express the radiant intensity I_ν as a linear function of the equivalent blackbody temperature T_{BB}. However, as discussed, for example, in Han and Westwater (2000), the RJA is only valid if $\hbar c \ll k_B T_{BB}$ with the Planck constant $\hbar$, the vacuum speed of light c, and the Boltzmann constant k_B. For high frequencies like 225 GHz and very low temperatures like the cosmic background temperature T_c of 2.725 K, the RJA needs to be replaced by the inverse of the Planck function B_ν^{-1}, which leads to the definition of brightness temperature as $T_B \equiv B_\nu^{-1}(I_\nu)$. For all radiometers used in this study their measured intensities are converted into T_B using the inverse Planck function and thus we can derive the optical thickness directly in terms of radiant intensities with

$$\tau = \ln\left[\frac{B_\nu(T_{mr}) - B_\nu(T_c)}{B_\nu(T_{mr}) - B_\nu(T_B)}\right]. \tag{7}$$

The frequency-specific mean radiative temperature T_{mr} is defined similar to Han and Westwater (2000) as

$$T_{mr} = B_\nu^{-1}\left\{\frac{\int_0^\infty B_\nu[T(z)]e^{-\tau(0,z)}\beta(z)\, dz}{1 - e^{-\tau(0,\infty)}}\right\}, \tag{8}$$

where $\beta(z)$ is the volume absorption coefficient of the atmospheric layer at height z and $\tau(0, \infty)$ denotes the opacity from ground level to the top of the atmosphere. The quantity T_{mr} has been directly derived from radiosonde profiles using an updated version of the monochromatic radiative transfer model (MonoRTM; Payne et al. 2011) for the SMT data. For the FKB and UFS sites, T_{mr} has been obtained from a statistical retrieval based on 2-m temperature and a long time series of radiosonde profiles (similar to, e.g., Mätzler and Morland 2009). The accuracy of T_{mr} using these methods is estimated to be better than 3 K, which has only a very small effect on the derived τ of less than 1%. In fact, we found that because of the comparably high values of T_{mr} for our frequency range and atmospheric conditions, T_{mr} can also be derived with sufficient accuracy using the RJA in (8). However, the conversion of the radiometer intensities into T_B and the contribution of T_c should always be calculated with B_ν^{-1} to avoid systematic errors at higher frequencies.

In this study, we concentrated on supercooled single-layer clouds with cloud thicknesses less than 2 km. The cloud boundaries were estimated by analyzing collocated cloud radar and lidar observations. The analysis was further restricted to clouds with maximum 35-GHz radar reflectivity of less than 0 dBZ to avoid too-high ice water contents that might contaminate the MWR data. A more detailed discussion of the influence of ice

particles on the MWR observations is given later in this section. Approximately 75% of the analyzed cloud cases have cloud thicknesses less than 1 km and in 34% of the data the clouds are thinner than 500 m. The temperature within the cloud is assumed to be equal to a constant mean cloud temperature $T_{\rm cld}$ derived from the estimated cloud boundaries and temperature profile information. For the SMT site, we found several cases of thin, single-layer mixed-phase clouds close to the ground. For those cases, where the liquid water layer could be well identified to be only at the cloud top using collocated lidar observations, $T_{\rm cld}$ has been assigned to the cloud-top temperature. The assumption of a constant $T_{\rm cld}$ simplifies (6) to

$$\tau_L = \mathrm{LWP}\alpha_L(\nu, T_{\rm cld}), \tag{9}$$

with the liquid water path $\mathrm{LWP} = \int_{z_{\rm cb}}^{z_{\rm ct}} \rho_L(z)\,dz$ and heights of cloud bottom $z_{\rm cb}$ and cloud top $z_{\rm ct}$. In addition to an independent estimate of LWP for deriving α_L, we also need to quantify the gaseous atmospheric contributions τ_D and $\tau_{\rm WV}$ since only the sum of all atmospheric components can be derived as τ using the MWR observations and (7).

A very elegant approach to disentangle the contribution from liquid cloud water and the gaseous constituents is to utilize their different temporal variability (Mätzler et al. 2010). Comparing T_B time series of ground-based MWR observations in clear-sky and cloudy situations reveals that cloud liquid water is the main reason for rapid changes in the observed T_B. The close correlation of fast opacity changes and liquid water fluctuations is illustrated in Fig. 3. A 10-min time period of derived opacities at 150 and 31.4 GHz with 4-s temporal resolution from the UFS site is shown as a scatterplot. The cloud considered here had a maximum thickness of 750 m with an average $T_{\rm cld}$ of −23°C; the cloud bottom was at the height of the UFS site. The measured opacities are nicely aligned along a straight line in the $\tau_{150} - \tau_{31.4}$ space. To validate whether the opacity changes are due to liquid water or water vapor fluctuations within the cloud, we calculated the range of opacity values for LWP up to 270 g m^{-2} with (9) and for a constant $T_{\rm cld}$ using the RAY model. For this particular temperature and frequency combination, the slope of the predicted opacities from the RAY model fits the measured opacities extremely well.

Even though the typical time scale of water vapor variability can be assumed to be much longer than 10 min for nonconvective conditions, we have to consider the influence of water vapor fluctuations that might be correlated with the liquid water fluctuations because of internal cloud processes like, for example, evaporation or

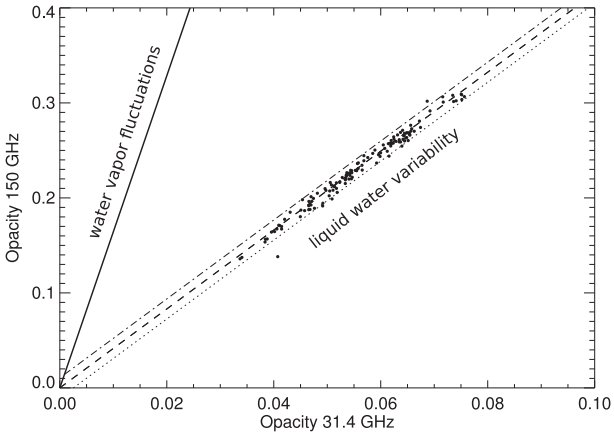

FIG. 3. Example of opacity variations at 150 and 31.4 GHz measured within a 10-min time period (4-s resolution) at the UFS site at 2150 UTC 14 Feb 2009. The fast opacity changes are mainly due to liquid water fluctuations (in the range of 200 g m^{-2}) with a 750-m-thick cloud layer (average cloud temperature $T_{\rm cld}$ = −23°C). The relationship between the opacities of the two channels predicted by the RAY model for solely liquid water fluctuations is shown by the dashed line. The solid line denotes the effect of only water vapor fluctuations predicted by the model from Rosenkranz (1998). The impacts of water vapor fluctuations in the range of up to 0.5 kg m^{-2} that are perfectly correlated (anticorrelated) with the liquid water fluctuations are indicated as dashed–dotted (dotted) lines.

condensation of cloud droplets (Mätzler et al. 2010). The solid line in Fig. 3 has been obtained assuming solely water vapor fluctuations within the cloud (constant $T_{\rm cld}$, constant pressure, no SLWP) using the water vapor absorption model from Rosenkranz (1998). The water vapor slope is much steeper compared to the liquid water slope, which is a necessary condition to be able to distinguish between water vapor and liquid water fluctuations. The dashed–dotted (dotted) lines in Fig. 3 also illustrate how the linear liquid water relationship would change if we assume that the liquid water fluctuations are perfectly correlated or anticorrelated with water vapor fluctuations in the range of 0.5 kg m^{-2} integrated water vapor content (IWV). The resulting uncertainty range due to water vapor fluctuations almost entirely covers the range of scatter in the data. However, it is likely that the scatter is also due to instrument noise or variability in cloud liquid water temperature.

Although we restricted our selection of clouds to nonprecipitating cases, we did not completely exclude mixed-phase clouds. Large ice and snow particles have been found to enhance the T_B observations at frequencies larger than 90 GHz because of scattering of the surface thermal emission back to the ground-based MWR (Kneifel et al. 2010). Thus, we also have to investigate the effect of potentially correlated ice water content (IWC) fluctuations on the derived opacities.

Since the contribution of SLW to the cloud radar signal at 35 GHz can be neglected with respect to ice particles, we estimated the cloud IWC with the temperature dependent method provided in Hogan et al. (2006). The maximum ice water path (IWP) has been found to be 2 (5) g m^{-2} at the UFS (SMT) site. According to the results in Kneifel et al. (2010), Löhnert et al. (2011), and Kneifel (2011), the T_B enhancement due to the maximum IWP can be estimated to be 0.06 (0.3) K at 90 (150) GHz for the UFS dataset. For the largest IWP found in the SMT data, we can similarly estimate the maximum T_B enhancement to be 0.15 (0.75) K at 90 (150) GHz and 1.25 K at 225 GHz. Even though radar estimates of IWC are generally affected by large uncertainties, the T_B enhancements even at 225 GHz are in the range of radiometric noise and are thus not a critical source of error for this analysis.

Assuming the fast opacity changes $\Delta\tau$ to be only due to liquid water changes ΔLWP, we can write

$$\Delta\tau_L(\nu, T_{\mathrm{cld}}) = \Delta\mathrm{LWP}\alpha_L(\nu, T_{\mathrm{cld}}). \quad (10)$$

Thus, the problem of determining $\alpha_L(\nu, T_{\mathrm{cld}})$ reduces to the problem of finding an independent estimate of ΔLWP. MWR retrievals of LWP are not suitable since a certain permittivity model has already been assumed for the generation of the LWP retrieval itself. For thin clouds with small LWP up to 60 g m^{-2}, an independent measure of LWP can be derived from infrared spectroscopy (Cadeddu and Turner 2011; Turner 2005). However, the restriction to small LWP values limits the analysis to comparably low signals in the MWR observations, especially at 31 GHz.

If no independent LWP estimate is available, then the absolute value of α_L cannot be derived in the described way. However, the MWR observations can be used to constrain existing permittivity models particularly if the MWR observations cover a wide spectral range. The fast opacity changes at two different frequencies can be used to derive the opacity ratio γ_{ν_1,ν_2} (Mätzler et al. 2010):

$$\gamma_{\nu_1,\nu_2} = \frac{\Delta\tau_L(\nu_1)}{\Delta\tau_L(\nu_2)} = \frac{\Delta\mathrm{LWP}\alpha_L(\nu_1)}{\Delta\mathrm{LWP}\alpha_L(\nu_2)} = \frac{\alpha_L(\nu_1)}{\alpha_L(\nu_2)}. \quad (11)$$

The dependence of all variables on T_{cld} is not explicitly written for better readability. The ratio of fast opacity changes at two frequencies γ_{ν_1,ν_2} is thus independent of LWP and equal to the ratio of the liquid water mass absorption coefficients. The quantity γ_{ν_1,ν_2} can be directly derived as the slope of a linear fit to the observations in an opacity scatterplot like the example in Fig. 3. This slope can be directly compared to the predicted ratio of mass absorption coefficients from the permittivity models. Even though the opacity ratios lack the information about the absolute value of α_L, γ_{ν_1,ν_2} can be used to validate the permittivity models, particularly if the observations cover a sufficiently wide spectral range and the critical low-temperature region.

The MWR observations (only zenith direction) from all sites have been subdivided into 10-min periods. The temporal resolution of the MWRs ranges from 1 to 3 s. Thus, the data from the different MWRs have been first matched and then averaged onto 4-s time intervals. The slope γ_{ν_1,ν_2} has been derived for the resulting data points (around 150 per 10-min temporal bin) with a least squares linear fit. The opacity values on both axes of the scatterplot are affected by errors that are difficult to estimate since atmospheric influences like variations in T_{cld} and correlated water vapor fluctuations affect the opacities as well as instrument noise or uncertainties in the estimated T_{mr}. For linear regression problems with unknown error in both variables, Clarke and Van Gorder (2013) recently presented a method on how the quality of the fit can be assessed. The slope from a classical least squares fit can be biased depending on whether $\tau_L(\nu_1)$ is fitted against $\tau_L(\nu_2)$ or vice versa. A better estimate of the true slope can be obtained from the geometric mean of γ_{ν_1,ν_2} and $\gamma^{-1}_{\nu_1,\nu_2}$. We utilized the supplemental material provided in Clarke and Van Gorder (2013) to ensure that only slope estimates that are within the 99% confidence interval of the true slope are accepted.

A specific advantage of the opacity ratio method is that constant biases in the derived opacity values—for example, due to instrument calibration errors—do not affect the slope estimate. In contrast, an erroneous gain calibration would strongly affect γ_{ν_1,ν_2} but the frequent gain calibration update performed by all MWR ensures that γ_{ν_1,ν_2} is a very robust measured quantity.

4. Results and discussion

We selected 10 frequency combinations between 31 and 225 GHz in a way to cover the entire observed spectral range but also to avoid frequencies within spectral regions of strong absorption bands. Thus, we only used the 31.4-GHz channel from the HATPRO instruments for K band (water vapor absorption line at 22.24 GHz) and only the 52.28-GHz channel in the V band (oxygen absorption band at 60 GHz). The measured opacity ratios for the three sites are presented together along with the various model estimates as function of T_{cld} down to −35°C in Figs. 4 and 5. The varying number of data points for the different frequency combinations is related to the dependence of the linear fit quality on the liquid water sensitivities in the

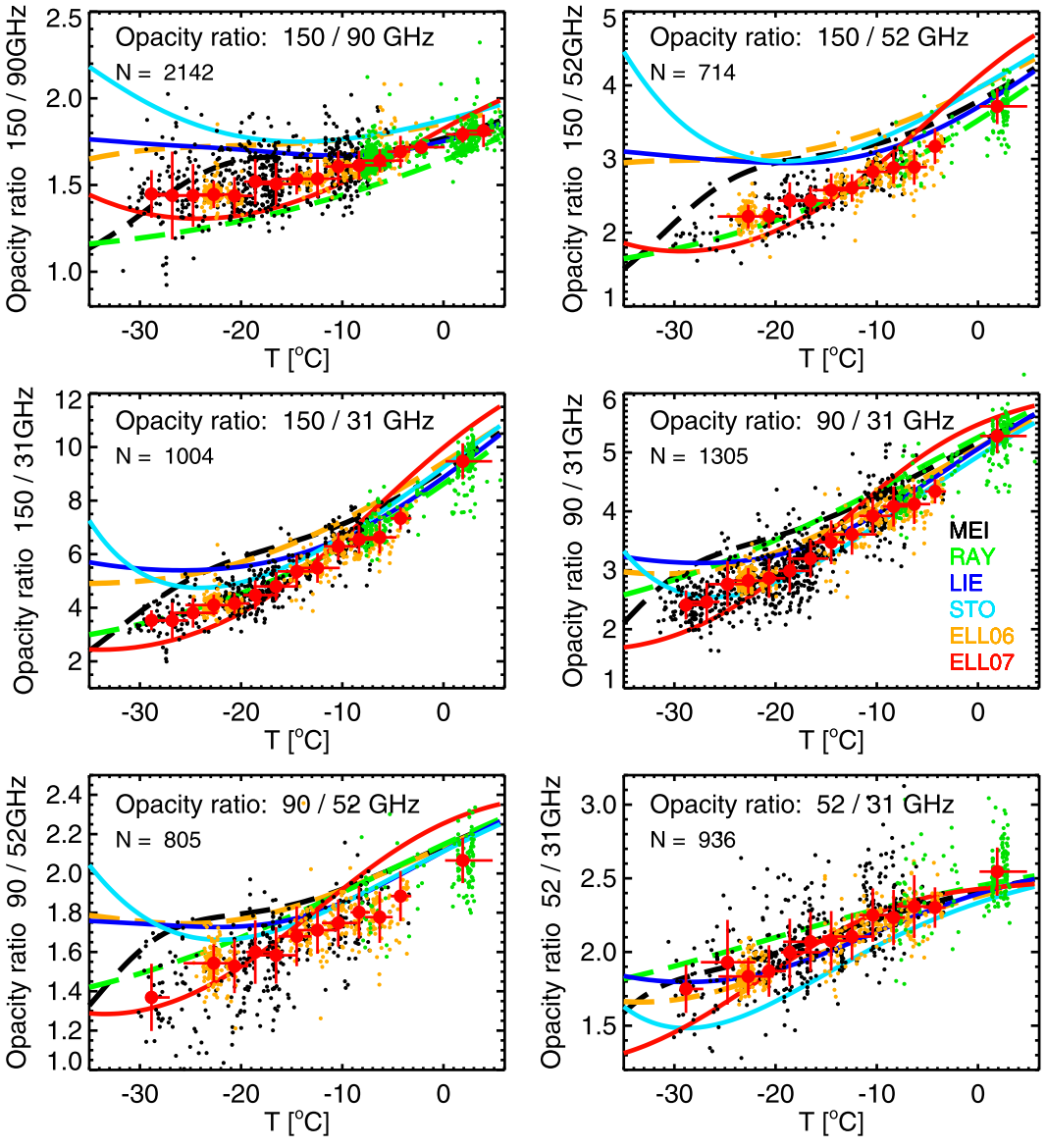

FIG. 4. Ratios of fast opacity changes (similar to the example slope in Fig. 3) for the frequency combinations (top left) 150/90 GHz, (top right) 150/52 GHz, (middle left) 150/31 GHz, (middle right) 90/31 GHz, (bottom left) 90/52 GHz, and (bottom right) 52/31 GHz as function of average cloud temperature (°C). Measured opacity ratios are shown as colored dots from three sites: SMT (black), UFS (orange), and FKB (green). The colored lines indicate the ratio of liquid water mass absorption coefficients predicted by the six permittivity models (Table 1 and Fig. 1), which are equal to the opacity ratios for pure liquid water opacities. Error estimates for the measured opacity ratios have been determined for each data point. For better readability of the plots all observations including error bars have been binned into 2.5°C temperature bins (red filled circles). The error in the estimation of T_{cld} (red x-error bars) and the variability of derived opacity ratios (red y-error bars) is shown as the standard deviation of the errors within each bin with at least 20 data points.

different channels, as well as on the individual noise characteristics of each channel.

a. Opacity ratios up to 150 GHz

For the six opacity ratios up to 150 GHz (150/90, 150/52, 150/31, 90/31, 90/52, and 52/31 GHz), observations from all three sites are available and are presented together in Fig. 4. The observations from the three sites and at all frequency combinations are found to be highly consistent with each other. This high consistency of the derived opacity ratios is strong evidence for the robustness of the method and the reliability of the derived

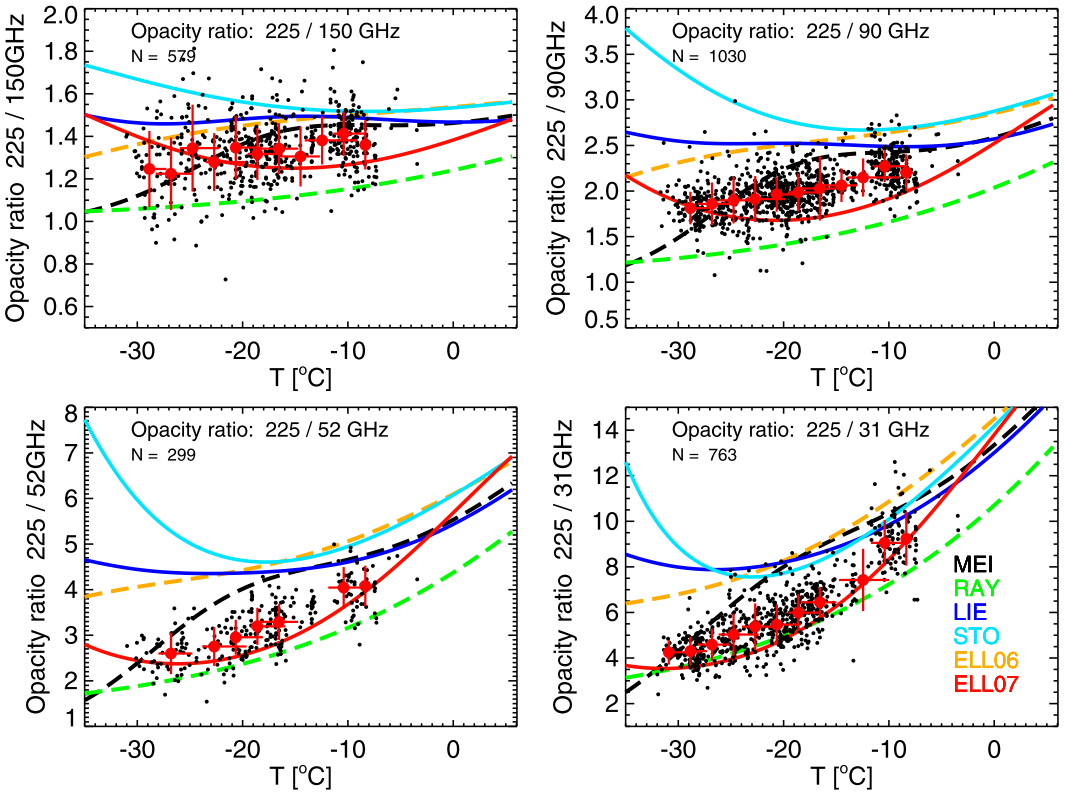

FIG. 5. As in Fig. 4, but for opacity ratios including 225 GHz, which are only available from SMT site: (top left) 225/150 GHz, (top right) 225/90 GHz, (bottom left) 225/52 GHz, and (bottom right) 225/31 GHz.

values, given that the data come from different instruments, site locations, and cloud types.

Considering the different permittivity models, we find the smallest spread among the modeled opacity ratios at lower frequencies and higher temperatures. This behavior is expected from Fig. 1 as the simulated opacity ratios are equal to the ratios of mass absorption coefficients at the two frequencies considered and the corresponding temperature. At temperatures below −20°C the deviations between the models strongly increase. Some of the modeled opacity ratios reveal significant features like a strong increase in the ratio for temperatures lower than −25°C with the STO model; very different behavior is seen in the MEI model.

When comparing the observed ratios with the model estimates, we find that the range of ratios predicted by the permittivity models largely covers the range of data in the observed ratios. This might be interpreted as evidence that the general choice of a Debye model and the temperature-dependent Debye parameters is a reasonable concept for the supercooled region. In the "safe" temperature region around 0°C, the observations match the model estimates relatively well. The few outliers are most likely due to the increasing magnitude of correlated water vapor fluctuations at higher temperatures at the lower altitude of the FKB site. The lower-frequency ratios including the 52.28-GHz channel (90/52 and 52/31 GHz) show a larger number of outliers and scatter. This might be related to the general smaller T_B variation due to liquid water at lower frequencies but also due to nonnegligible influence of the oxygen absorption band at 60 GHz on the 52.28-GHz channel, which causes a higher sensitivity of this channel to temporal changes of the air temperature profile.

To compare the observed ratios with the model estimates in a more quantitative way, we calculate a normalized root-mean-square deviation (NRMSD) expressed in percent for each frequency combination as

$$\mathrm{NRMSD} = 100 \times \frac{\sqrt{\dfrac{\sum_{i=1}^{N} [\gamma_{\mathrm{mod}}(T_i) - \overline{\gamma_{\mathrm{obs}}(T_i)}]^2}{N}}}{\max(\overline{\gamma_{\mathrm{obs}}}) - \min(\overline{\gamma_{\mathrm{obs}}})}. \quad (12)$$

The observed ratios are binned into 2.5°C temperature bins T_i containing at least 20 observations per bin. The root-mean-square deviation (RMSD) is calculated with the bin-averaged observed ratios $\overline{\gamma_{\mathrm{obs}}(T_i)}$ (shown as

TABLE 3. NRMSD between observed opacity ratios (temperature binned) and the various permittivity model estimates as defined in (12) in percent. Boldface numbers indicate minimum NRMSD values for the different frequency combinations. The rightmost column (OBS) contains the mean standard deviation of the observed, temperature-binned opacity ratios normalized by the maximum difference of the ratios at each frequency combination similar to (12) in percent.

Opacity ratio	MEI	RAY	LIE	STO	ELL06	ELL07	OBS
225/150 GHz	**41.2**	117.0	86.0	137.6	69.8	50.0	74.9
225/90 GHz	**52.2**	119.9	114.1	191.2	110.5	56.6	48.3
225/52 GHz	55.5	47.4	84.5	113.3	90.5	**26.0**	28.5
225/31 GHz	34.7	20.1	52.8	55.3	49.3	**15.6**	17.7
150/90 GHz	**27.1**	44.4	47.4	74.7	54.8	29.4	28.7
150/52 GHz	33.2	**7.4**	30.5	37.4	42.8	21.4	13.8
150/31 GHz	19.6	**3.9**	18.7	13.6	21.4	12.5	8.8
90/31 GHz	18.3	17.6	11.9	**5.3**	11.9	14.3	10.9
90/52 GHz	29.0	**20.4**	24.2	21.9	29.4	22.2	19.3
52/31 GHz	**7.8**	16.0	9.8	29.1	10.9	14.7	23.5
All	31.8	41.4	48.0	67.9	49.1	**26.3**	27.4

filled red circles in Figs. 4 and 5) and the ratios $\gamma_{\mathrm{mod}}(T_i)$ predicted by the permittivity models; for better readability the two frequency indices in the opacity ratios have been omitted in (12). The total number of valid temperature bins per frequency combination is N. To make the RMSD from different frequency combinations comparable, the RMSD is also normalized by the maximum difference of $\overline{\gamma_{\mathrm{obs}}}$ at each specific frequency combination. The resulting NRMSD values for all frequency combinations and permittivity models are presented in Table 3. We also included in Table 3 the mean standard deviation of the observed, temperature-binned opacity ratios normalized by the maximum difference of the opacity ratios at each frequency combination similar to the definition of NRMSD. These values can be interpreted as a measure of the uncertainty of the observations.

Considering the resulting NRMSD, one finds the lowest values for the MEI model at 150/90 GHz and 52/31 GHz; for the RAY model at 150/52 GHz, 150/31 GHz, and 90/52 GHz; and for the STO model at 90/31 GHz. The models LIE, ELL06, and ELL07 show larger NRMSDs for all six frequency combinations compared to the remaining models. The variability of NRMSD between the permittivity models for one specific frequency combination is also considerably different. While, for example, at 90/52 GHz the NRMSD values range only between 20.4% and 29.4%, the lowest value at 90/31 GHz is found with 5.3% for STO, which is over 3 times smaller compared to the largest value of 18.3% found for MEI. In addition to the NRMSD it is also important to compare the overall temperature dependence of the observations and the permittivity model estimates: Even though the MEI model shows the lowest NRMSD for three of the six frequency combinations, the general decrease of opacity ratios at temperatures below −20°C seems to be in contradiction to the observations. In a similar way this is true for the strong increase of opacity ratios for STO at temperatures below −20°C.

Based on either the NRMSDs or the more qualitative consideration of the temperature dependence, there does not appear to be a ''golden'' model that suitably fits the observations at all six frequency combinations in Fig. 4. For example, the RAY model provides a surprisingly good fit to the 150/31-GHz ratios (NRMSD of 3.9%) but it is systematically overestimating the ratios at 90/31 GHz. The newest ELL07 model is able to fit the data rather well at temperatures below −10°C but shows a tendency to overestimate the ratios at higher temperatures resulting in comparably large NRMSDs.

b. *Opacity ratios including 225 GHz*

Opacity ratios that include observations at 225 GHz (225/150 GHz, 225/90 GHz, 225/52 GHz, 225/31 GHz) are only available from the SMT site in Greenland and are shown in a similar way as for the lower frequencies in Fig. 5. Similar to Fig. 4, the models increasingly deviate from each other with decreasing temperatures, but again the observed values are found to be in between the various model predictions. Interestingly, the STO model lies almost entirely outside the measured range at the four 225-GHz ratios, while it was within the range of the observation for the lower-frequency opacity ratios in Fig. 4. As a result, the STO model has the largest NRMSDs for the four 225-GHz ratios. Similar to the lower-frequency ratios, STO exhibits a strange ''hook feature'' with increasing ratios at the lowest temperatures. This unnatural behavior can be found in all frequency combinations with varying temperature dependence but it is most prominent in the 225/90-, 225/52-, and 225/31-GHz ratios. In contrast, the MEI model shows strongly decreasing opacity

ratios at lower temperatures that cannot be found in the other models; this was also seen in the lower-frequency ratios in Fig. 4. The LIE and ELL06 models tend to overestimate the opacity ratios; however, this overestimate is more moderate and does not have the unnaturally strong increasing/decreasing features at the lowest-temperature region that other models have. Unlike all other models, the RAY model significantly underestimates the opacity ratios for these higher frequencies (Fig. 5). The ELL07 model fits all four observed opacity ratios reasonably well and provides the closest fit to the data at 225/52 GHz and 225/31 GHz with NRMSDs of 26% and 15.6%, respectively. At the two higher-frequency combinations of 225/150 and 225/90 GHz, the ''bending up'' of the ELL07 model at the lowest temperatures is not supported by the observations and thus the NRMSDs are slightly larger compared to the lowest values produced by MEI. However, the low number of observations at temperatures below −30°C and the comparably large uncertainties in the observed opacity ratios at particularly 225/150 and 225/90 GHz does prevent us from determining if the increase of opacity ratios at temperatures lower than −30°C and these specific frequency combinations is statistically significant.

c. *Implication for mass absorption coefficient*

The opacity ratios at the 10 different frequency pairs clearly illustrate the need for the observations to cover a wide spectral range to evaluate the performance of permittivity models with opacity ratios. For example, a certain model might be able to fit a single opacity ratio over the temperature range well (e.g., the RAY model at 150/31 GHz), but its underlying mass absorption values might be completely erroneous. If we could identify a ''golden model'' that is able to fit all of the opacity ratios well over the supercooled temperature range, it would be unlikely that it predicts entirely incorrect mass absorption values.

The motivation in section 3 to derive opacity ratios was their independence of LWP observations. However, α_L can be determined if we are able to accurately specify the temperature dependence of a certain $\alpha_L(\nu_{\text{ref}}, T)$ at a specific frequency ν_{ref} throughout the entire supercooled temperature region. If the reference frequency ν_{ref} is also included in the measured opacity ratios $\gamma_{\nu,\nu_{\text{ref}}}(T)$, then we can simply derive the unknown $\alpha_L(\nu, T)$ with

$$\alpha_L(\nu, T) = \gamma_{\nu,\nu_{\text{ref}}}(T)\alpha_L(\nu_{\text{ref}}, T). \tag{13}$$

Cadeddu and Turner (2011) found in their direct comparison of measured α_L with model prediction the STO model to fit their observations best, especially at 90 GHz. Our opacity ratio comparison (Fig. 4 and Table 3) revealed that STO fits the ratios at 90/31 GHz extremely well. It might seem to be contradictory, however, that STO fails to provide a good fit to the other two low-frequency ratios at 90/52 and 52/31 GHz. As discussed earlier, the 52.28-GHz channel observations are problematic because of the influences of the close oxygen band; this influence can also be found in the by a factor of 2 larger uncertainties of these opacity ratios. Our selection of the STO model at 90 GHz as our reference model $\alpha_L(90, T)$ is therefore mainly based on the findings in Cadeddu and Turner (2011) since model errors could easily cancel out for a single opacity ratio. Assuming an error of 10% for $\alpha_L(90, T)$ and using the error estimates for the bin-averaged observations of $\gamma_{\nu,90}$, the resulting $\alpha_L(\nu, T)$ and its associated error for 31.4, 52.28, 150, and 225 GHz can be calculated (Fig. 6).

At 31.4 GHz, the STO model is found to fit the derived α_L extremely well, which is in agreement with the findings in Mätzler et al. (2010) and Cadeddu and Turner (2011). This consistent finding for 31.4 GHz is particularly important since 31.4 GHz is a common frequency used to retrieve SLWP. Considering the large deviations of the various permittivity models at 31.4 GHz, which can potentially lead to large SLWP retrieval biases (Fig. 2), the results suggests that the STO model should be preferred for temperatures down to −30°C in retrieval development and MW radiative transfer. Since our data are for temperatures above −30°C, we are unable to state which model is more accurate for cloud temperatures below this threshold. Relative to the STO model, all other models (especially MEI and RAY) increasingly overestimate $\alpha_L(31.4, T)$ with decreasing temperature. This implies that SLWP retrievals using other permittivity models than STO are likely to underestimate the true SLWP amounts of observed clouds at temperatures below −15°C.

At 52.28 GHz, the STO model is found to be still close to the derived α_L; however, as discussed before, the larger scattering in the 90/52-GHz ratio leads also to larger error bars of the derived α_L and the opacity ratios including 52.28 GHz should be interpreted carefully. In general, the observations provide an indication that the STO model might be the currently best choice for frequencies up to 90 GHz. At higher frequencies (150 and 225 GHz) the STO model is similar to the LIE, ELL06, and MEI models in that it increasingly overestimates the α_L values. The only model that fits the absolute values and the general temperature dependence of α_L at these higher frequencies is ELL07. Thus, at frequencies larger than 90 GHz up to 225 GHz, the ELL07 model seems to provide the most realistic estimates of α_L.

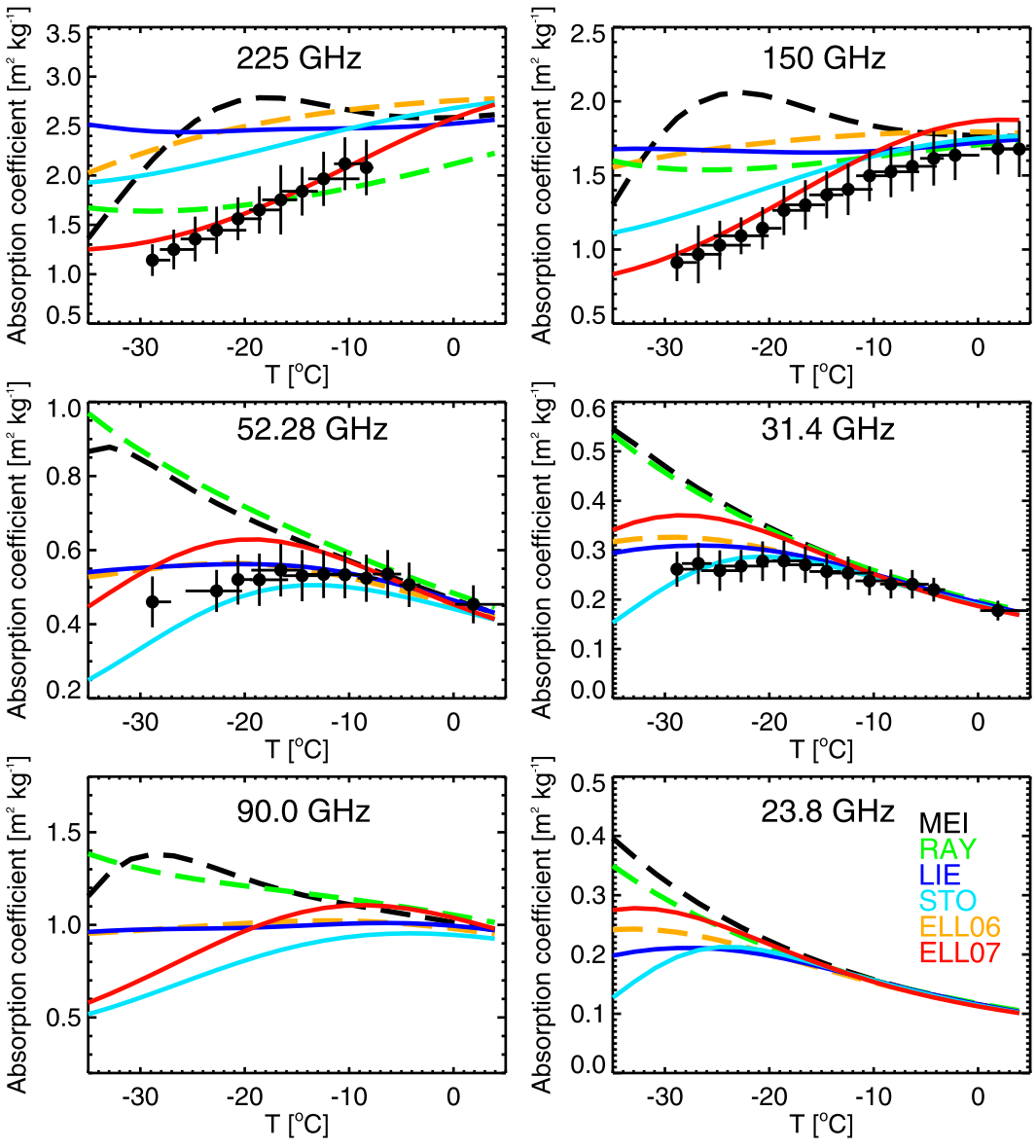

FIG. 6. Liquid water mass absorption coefficient ($m^2\,kg^{-1}$) as function of liquid water temperature (°C) for (top left) 225, (top right) 150, (middle left) 52.28, (middle right) 31.4, (bottom left) 90, and (bottom right) 23.8 GHz. The colored lines are the predicted values of the six permittivity models described in Table 1. The black filled circles (top two panels) are mass absorption coefficients derived according to (13) using the binned measured opacity ratios 225/90, 150/90, 52/90, and 90/31 GHz shown in Figs. 4 and 5 and the STO model at 90 GHz (light blue line in bottom-left panel) as reference model for $\alpha_L(90, T)$. Error bars in the y direction of the observations include the uncertainty of the derived opacity ratios and an assumed uncertainty of 10% for the reference model (STO) for $\alpha_L(90, T)$. The bottom-left panel shows the temperature dependence of the reference model (STO) at 90 GHz; the bottom-right panel illustrates the model spread at 23.8 GHz, which is often used in combination with 31.4 GHz for SLWP retrievals.

5. Conclusions

In this study, we applied a recently proposed method to utilize ground-based MWR observations of supercooled liquid clouds to evaluate the accuracy and spectral consistency of different permittivity models for supercooled liquid water. The different time scales of fluctuations in liquid water and atmospheric gases allow the derivation of liquid water opacities. Ratios of these opacities at two different frequencies are independent of SLWP and equal to the ratios of mass absorption coefficients that can be directly derived from permittivity

models. We used observations between 31 and 225 GHz from different ground-based MWR located at three sites in Greenland, the German Alps, and southwest Germany to evaluate six permittivity models over a wide range of supercooled liquid water clouds. Cloud radar and lidar observations are used to estimate the cloud boundaries. Together with radiosondes and model analysis data, the average SLW temperature and its uncertainty range was derived. The final dataset[1] contains a unique collection of supercooled clouds from different climatic regions including average cloud temperatures between −33° and +5°C.

The derived opacity ratios from the different sites–instruments show a remarkably high consistency to each other, which indicates the robustness of the method and the reliability of the derived opacity ratios. The comparison of the observed ratios with six permittivity models also reveals the following:

- The range of opacity ratios predicted by the six permittivity models is generally able to cover the majority of observed ratios. The deviations between the models themselves and between models and observations are smallest at temperatures close to 0°C; they dramatically increase at cloud temperatures lower than approximately −15°C (depending on frequency combination).
- Although certain models are found to provide almost a perfect fit to the observed opacity ratios at specific frequency combinations, no model was identified that provides a sufficiently accurate approximation to the observations over the entire spectral range and cloud temperature range.
- The STO, LIE, and ELL06 models systematically overestimate the observed opacity ratios if frequencies higher than 90 GHz are included. The RAY model tends to underestimate the opacity ratios particularly for the ratios including 225 GHz. The most recent model by ELL07 is found to be the best approximation at temperatures below −10°C but tends to overestimate the opacity ratios at higher temperatures between −10° and +5°C.

The clear advantages of the opacity ratio method are its independence of an accurate and independent estimate of SLWP and its robustness in the face of possible MWR calibration offsets. A disadvantage of the approach is the loss of information about the absolute value of the mass absorption coefficient. Hence, the performance of the permittivity models can only be evaluated if a broad range of frequencies and temperatures is considered. For most applications (e.g., SLWP retrievals or estimation of cloud radar attenuation due to SLW), the absolute value of the mass absorption coefficient $\alpha_L(\nu, T)$ is required.

By combining the measured opacity ratios with a reference α_L at 90 GHz (STO), which is based on the findings in Cadeddu and Turner (2011), the mass absorption coefficients at 31.4, 52.28, 150, and 225 GHz as function of temperature were derived. The resulting α_L are clearly limited by the uncertainties in the reference $\alpha_L(90, T)$ and the related uncertainties in the observed opacity ratios. Despite the remaining uncertainties of the method we can draw a few important conclusions about the applicability of the six permittivity models for frequencies between 31.4 and 225 GHz:

- Consistent with our comparisons in the opacity ratio space, none of the investigated permittivity models were able to sufficiently approximate the observed mass absorption values at all four frequencies (31.4, 52.28, 150, and 225 GHz) over the entire temperature range.
- For liquid water temperatures down to −30°C and frequencies lower than 90 GHz, the STO model has the best agreement with the observations. This finding is in general agreement with Mätzler et al. (2010) and Cadeddu and Turner (2011), and thus we suggest that the STO model be used for SLW retrieval development and MW radiative transfer in this specific frequency/temperature region.
- For frequencies larger than 90 GHz (particularly 150 and 225 GHz), we find the ELL07 model superior; the majority of the remaining models tend to overestimate α_L at these higher frequencies for temperatures down to −30°C.

Our study has shown the potential of ground-based MWR observations that cover a broad spectral range and a range of supercooled cloud temperature to evaluate liquid water permittivity models. However, to substantially improve the liquid water permittivity models in the supercooled temperature region and over a wide spectral range (e.g., 1–1000 GHz), more laboratory data are required. As shown in (1), the absorption index that can be derived from MWR observations is dependent both on the imaginary and real part of the complex permittivity. Only laboratory data are able to provide independent measurements of both parts of the complex permittivity to develop improved permittivity models. The ongoing activities to utilize higher MW frequencies in passive–active applications should lead to a renewed interest of the retrieval and cloud microphysics communities to perform extended laboratory studies in

[1] The opacity ratio dataset together with a short description of the STO model and Interactive Data Language (IDL) routines for the STO and ELL07 model are available on request from the corresponding author.

order to avoid systematic biases in current and future cloud retrieval products.

Acknowledgments. The data from the UFS site used in this study were collected as part of the TOSCA campaign, which has been funded by the German Science Foundation (DFG) under Grant LO 901/3-1. The radiosonde, cloud radar, and lidar observations at the FKB site were collected by the U.S. Department of Energy ARM's mobile facility as part of COPS; the MWR data at the FKB site have been collected during the GOP campaign, which has been funded by DFG under Grant WU 356/4-2. ICECAPS is supported by the U.S. National Science Foundation under Grants ARC-0856773, 0904152, and 0856559 as part of the Arctic Observing Network (AON) program, with additional instrumentation support provided by the NOAA Earth System Research Laboratory, ARM, and Environment Canada. ICECAPS data are available via the ARM data archive. Argonne National Laboratory's work was supported by the U.S. Department of Energy, Office of Science, under Contract DE-AC02-06CH11357. Research done by Stefan Kneifel and Stephanie Redl has been carried out within the Hans Ertel Centre for Weather Research. Climate Monitoring Branch. Contributions from Emiliano Orlandi have been financed by the DFG priority program High Altitude and Long Range Research Aircraft [HALO (SPP 1294) Project: Using the HALO Microwave Package (HAMP) for cloud and precipitation research, GZ: CR 111/9-1]. The authors are also very grateful to Susanne Crewell (University of Cologne) for many fruitful discussions. Constructive comments from three anonymous reviewers are also gratefully recognized.

REFERENCES

Battaglia, A., and J. Delanoë, 2013: Synergies and complementarities of *CloudSat-CALIPSO* snow observations. *J. Geophys. Res. Atmos.,* **118,** 721–731, doi:10.1029/2012JD018092.

Bennartz, R., and Coauthors, 2013: July 2012 Greenland melt extent enhanced by low-level liquid clouds. *Nature,* **496,** 83–86, doi:10.1038/nature12002.

Bertolini, D., M. Cassettari, and G. Salvetti, 1982: The dielectric relaxation time of supercooled water. *J. Chem. Phys.,* **76,** 3285–3290, doi:10.1063/1.443323.

Boudala, F. S., G. A. Isaac, S. G. Cober, and Q. Fu, 2004: Liquid fraction in stratiform mixed-phase clouds from in situ observations. *Quart. J. Roy. Meteor. Soc.,* **130,** 2919–2931, doi:10.1256/qj.03.153.

Cadeddu, M. P., and D. D. Turner, 2011: Evaluation of water permittivity models from ground-based observations of cold clouds at frequencies between 23 and 170 GHz. *IEEE Trans. Geosci. Remote Sens.,* **49,** 2999–3008, doi:10.1109/TGRS.2011.2121074.

——, J. C. Liljegren, and D. D. Turner, 2013: The Atmospheric Radiation Measurement (ARM) Program network of microwave radiometers: Instrumentation, data, and retrievals. *Atmos. Meas. Tech. Discuss.,* **6,** 3723–3763, doi:10.5194/amtd-6-3723-2013.

Clarke, A. J., and S. Van Gorder, 2013: On fitting a straight line to data when the "noise" in both variables is unknown. *J. Atmos. Oceanic Technol.,* **30,** 151–158, doi:10.1175/JTECH-D-12-00067.1.

Cole, K. S., and R. H. Cole, 1941: Dispersion and absorption in dielectrics I. Alternating current characteristics. *J. Chem. Phys.,* **9,** 341–351, doi:10.1063/1.1750906.

Crewell, S., and U. Löhnert, 2003: Accuracy of cloud liquid water path from ground-based microwave radiometry: 2. Sensor accuracy and strategy. *Radio Sci.,* **38,** 8042, doi:10.1029/2002RS002634.

——, and Coauthors, 2008: The general observation period 2007 within the priority program on quantitative precipitation forecasting: Concept and first results. *Meteor. Z.,* **17,** 849–866, doi:10.1127/0941-2948/2008/0336.

Debye, P., 1929: *Polare Molekeln.* Hirzel, 200 pp.

Ellison, W., 2006: Dielectric properties of natural media. *Thermal Microwave Radiation: Applications for Remote Sensing,* C. Mätzler, Ed., The Institution of Engineering and Technology, 431–455.

——, 2007: Permittivity of pure water, at standard atmospheric pressure, over the frequency range 0–25 THz and the temperature range 0–100°C. *J. Phys. Chem. Ref. Data,* **36,** 1–18, doi:10.1063/1.2360986.

Evans, K. F., and G. L. Stephens, 1995: Microwave radiative-transfer through clouds composed of realistically shaped ice crystals. Part II: Remote sensing of ice clouds. *J. Atmos. Sci.,* **52,** 2058–2072, doi:10.1175/1520-0469(1995)052<2058:MRTTCC>2.0.CO;2.

Han, Y., and E. R. Westwater, 2000: Analysis and improvement of tipping calibration for ground-based microwave radiometers. *IEEE Trans. Geosci. Remote Sens.,* **38,** 1260–1276, doi:10.1109/36.843018.

Heymsfield, A. J., L. M. Miloshevich, A. Slingo, K. Sassen, and D. Starr, 1991: An observational and theoretical study of highly supercooled altocumulus. *J. Atmos. Sci.,* **48,** 923–945, doi:10.1175/1520-0469(1991)048<0923:AOATSO>2.0.CO;2.

Hogan, R. J., M. P. Mittermaier, and A. J. Illingworth, 2006: The retrieval of ice water content from radar reflectivity factor and temperature and its use in evaluating a mesoscale model. *J. Appl. Meteor. Climatol.,* **45,** 301–317, doi:10.1175/JAM2340.1.

Kneifel, S., 2011: Characterization of snowfall using ground-based passive and active remote sensors. Ph.D. thesis, University of Cologne, 115 pp. [Available online at http://kups.ub.uni-koeln.de/4566/.]

——, U. Löhnert, A. Battaglia, S. Crewell, and D. Siebler, 2010: Snow scattering signals in ground-based passive microwave radiometer measurements. *J. Geophys. Res.,* **115,** D16214, doi:10.1029/2010JD013856.

Liebe, H. J., G. H. Hufford, and T. Manabe, 1991: A model for the complex permittivity of water at frequencies below 1 THz. *Int. J. Infrared Millimeter Waves,* **12,** 659–675, doi:10.1007/BF01008897.

——, ——, and M. G. Cotton, 1993: Propagation modeling of moist air and suspended water/ice particles at frequencies below 1000 GHz. *Proc. AGARD*, **542,** 1–10.

Lipton, A. E., M. K. Griffin, and A. G. Ling, 1999: Microwave transfer model differences in remote sensing of cloud liquid

water at low temperatures. *IEEE Trans. Geosci. Remote Sens.,* **37,** 620–623, doi:10.1109/36.739129.

Löhnert, U., S. Kneifel, A. Battaglia, M. Hagen, L. Hirsch, and S. Crewell, 2011: A multisensor approach toward a better understanding of snowfall microphysics: The TOSCA project. *Bull. Amer. Meteor. Soc.,* **92,** 613–628, doi:10.1175/2010BAMS2909.1.

Mätzler, C., and J. Morland, 2009: Refined physical retrieval of integrated water vapor and cloud liquid for microwave radiometer data. *IEEE Trans. Geosci. Remote Sens.,* **47,** 1585–1594, doi:10.1109/TGRS.2008.2006984.

——, P. W. Rosenkranz, and J. Cermak, 2010: Microwave absorption of supercooled clouds and implications for the dielectric properties of water. *J. Geophys. Res.,* **115,** D23208, doi:10.1029/2010JD014283.

Meissner, T., and F. J. Wentz, 2004: The complex dielectric constant of pure and sea water from microwave satellite observations. *IEEE Trans. Geosci. Remote Sens.,* **42,** 1836–1849, doi:10.1109/TGRS.2004.831888.

Morrison, H., G. de Boer, G. Feingold, J. Harrington, M. D. Shupe, and K. Sulia, 2012: Resilience of persistent Arctic mixed-phase clouds. *Nat. Geosci.,* **5,** 11–17, doi:10.1038/ngeo1332.

Payne, V. H., E. J. Mlawer, K. E. Cady-Pereira, and J.-L. Moncet, 2011: Water vapor continuum absorption in the microwave. *IEEE Trans. Geosci. Remote Sens.,* **49,** 2194–2208, doi:10.1109/TGRS.2010.2091416.

Ray, P. S., 1972: Broadband complex refractive indices of ice and water. *Appl. Opt.,* **11,** 1836–1844, doi:10.1364/AO.11.001836.

Ronne, C., L. Thrane, P. Astrand, A. Wallqvist, K. V. Mikkelsen, and S. R. Keiding, 1997: Investigation of the temperature dependence of dielectric relaxation in liquid water by THz reflection spectroscopy and molecular dynamics simulation. *J. Chem. Phys.,* **107,** 5319–5331, doi:10.1063/1.474242.

Rose, T., S. Crewell, U. Löhnert, and C. Simmer, 2005: A network suitable microwave radiometer for operational monitoring of the cloudy atmosphere. *Atmos. Res.,* **75,** 183–200, doi:10.1016/j.atmosres.2004.12.005.

Rosenkranz, P. W., 1998: Water vapor microwave continuum absorption: A comparison of measurements and models. *Radio Sci.,* **33,** 919–928, doi:10.1029/98RS01182.

Shupe, M. D., 2011: Clouds at Arctic atmospheric observatories. Part II: Thermodynamic phase characteristics. *J. Appl. Meteor. Climatol.,* **50,** 645–661, doi:10.1175/2010JAMC2468.1.

——, and Coauthors, 2013: High and dry: New observations of tropospheric and cloud properties above the Greenland Ice Sheet. *Bull. Amer. Meteor. Soc.,* **94,** 169–186, doi:10.1175/BAMS-D-11-00249.1.

Stogryn, A. P., H. T. Bull, K. Rubayi, and S. Iravanchy, 1995: The microwave permittivity of sea and fresh water. Aerojet Internal Rep., GenCorp Aerojet, Azusa, CA, 24 pp.

Turner, D. D., 2005: Arctic mixed-phase cloud properties from AERI lidar observations: Algorithm and results from SHEBA. *J. Appl. Meteor.,* **44,** 427–444, doi:10.1175/JAM2208.1.

——, and Coauthors, 2007: Thin liquid water clouds: Their importance and our challenge. *Bull. Amer. Meteor. Soc.,* **88,** 177–190, doi:10.1175/BAMS-88-2-177.

——, U. Löhnert, M. Cadeddu, S. Crewell, and A. Vogelmann, 2009: Modifications to the water vapor continuum in the microwave suggested by ground-based 150 GHz observations. *IEEE Trans. Geosci. Remote Sens.,* **47,** 3326–3337, doi:10.1109/TGRS.2009.2022262.

Ulaby, F. T., R. K. Moore, and A. K. Fung, 1986: *From Theory to Applications,* Vol. 3, *Microwave Remote Sensing: Active and Passive,* Artech House, 1120 pp.

Wulfmeyer, V., and Coauthors, 2008: The Convective and Orographically Induced Precipitation Study: A research and development project of the World Weather Research Program for improving quantitative precipitation forecasting in low-mountain regions. *Bull. Amer. Meteor. Soc.,* **89,** 1477–1486, doi:10.1175/2008BAMS2367.1.